Macroscopic hyperpolarization enhanced with quantum optimal control

Alastair Marshall [1,2,*], Thomas Reisser [3,4,*], Phila Rembold [3,4,5,6,*], Christoph Müller,[1] Jochen Scheuer,[1] Martin Gierse,[1,2]
Tim Eichhorn,[1] Jakob M. Steiner [1,7], Patrick Hautle,[7] Tommaso Calarco,[3,4] Fedor Jelezko,[2] Martin B. Plenio,[8]
Simone Montangero [5,6,9] Ilai Schwartz,[1] Matthias M. Müller,[3] and Philipp Neumann[1]

[1]*NVision Imaging Technologies GmbH, D-89081 Ulm, Germany*

[2]*Institute for Quantum Optics (IQO) and Center for Integrated Quantum Science and Technology (IQST), Albert-Einstein-Allee 11,
Universität Ulm, D-89081 Ulm, Germany*

[3]*Forschungszentrum Jülich GmbH, Peter Grünberg Institute - Quantum Control (PGI-8), D-52425 Jülich, Germany*

[4]*Institute for Theoretical Physics, University of Cologne, D-50937 Cologne, Germany*

[5]*Dipartimento di Fisica e Astronomia "G. Galilei," Università degli Studi di Padova, I-35131 Padua, Italy*

[6]*Istituto Nazionale di Fisica Nucleare (INFN), Sezione di Padova, I-35131 Padua, Italy*

[7]*Paul Scherrer Institute, CH-5232 Villigen PSI, Switzerland*

[8]*Institute of Theoretical Physics (ITP) and Center for Integrated Quantum Science and Technology (IQST), Albert-Einstein-Allee 11,
Universität Ulm, D-89081 Ulm, Germany*

[9]*Padua Quantum Technologies Research Center, Università degli Studi di Padova, I-35131 Padua, Italy*

Hyperpolarization of nuclear spins enhances nuclear magnetic resonance signals, which play a key role for imaging and spectroscopy in the natural and life sciences. This signal amplification unlocks previously inaccessible techniques, such as metabolic imaging of cancer cells. In this paper, electron spins from the photoexcited triplet state of pentacene-doped naphthalene crystals are used to polarize surrounding protons. As existing strategies are rendered less effective by experimental constraints, they are replaced with optimal control pulses designed with REDCRAB. In contrast to previous optimal control approaches, which consider one or two effective nuclei, this closed-loop optimization is macroscopic. A 26% improvement in signal and 15% faster polarization rate are observed. Additionally, a strategy called autonomously optimized repeated linear sweep (ARISE) is introduced to efficiently tailor existing hyperpolarization sequences in the presence of experimental uncertainty to enhance their performance. ARISE is expected to be broadly applicable in many experimental settings.

I. INTRODUCTION

Sensitive nuclear magnetic resonance (NMR) spectroscopy and magnetic resonance imaging (MRI) are key drivers in research areas from life sciences through material science to quantum computing. The feasibility and sensitivity of such experiments critically depend on the polarization of the utilized spins. Dynamic nuclear polarization (DNP) techniques have been shown to increase NMR signals by multiple orders of magnitude [1], enabling previously inaccessible imaging techniques [2]. DNP transfers the polarization from highly polarized electron spins to a target species of nuclear spins [3] used for NMR protocols. Electron spins are polarized, for example, by thermalization at low temperatures and high magnetic fields or by optical polarization of atoms and suitable

molecules in gases, liquids, and solids [1,4–11]. In this paper, the electron spins of photoexcited triplet states in pentacene are used as the source of polarization, and the proton spins of naphthalene are used as the target. The final polarization of the sample is enhanced via the application of quantum optimal control (QOC) techniques to a dynamic nuclear polarization scheme in a closed-loop fashion. The efficiency of the overall proton polarization process is increased by optimizing the DNP transfer process using closed-loop QOC. To guide the algorithm towards a solution which produces a strongly increased signal, it is helpful to provide a good initial guess. Consequently, a new multistep protocol is introduced called autonomously optimized repeated linear sweep (ARISE). It provides a systematic approach to the improvement of "integrated solid effect"-like (ISE-like) linear sweep DNP sequences in the presence of an unknown experimental transfer function. The macroscopic properties of the polarized crystals have been further investigated in a separate publication [12] confirming an improved sample polarization of 25%.

Some background regarding the target quantum system and existing DNP strategies, as well as an introduction to QOC, is given in Sec. II. In Sec. III A the measurement techniques are explained in more detail, and a description of the
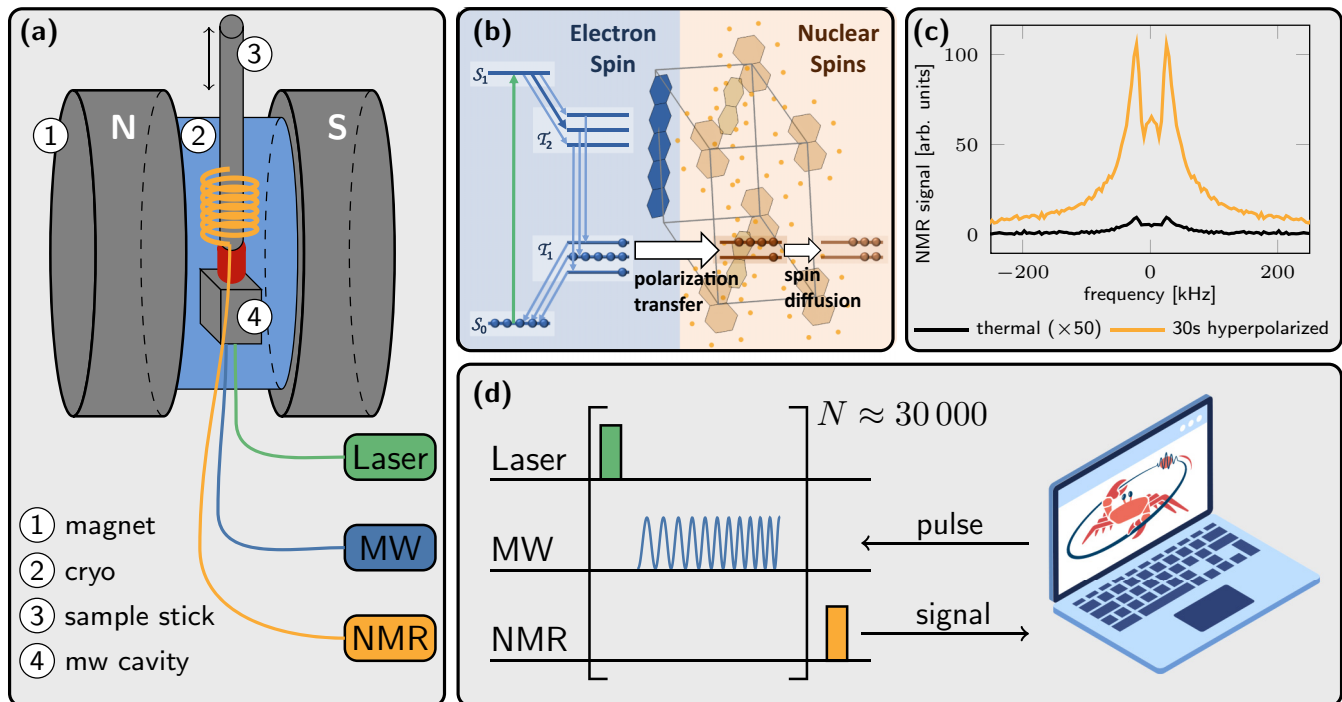

FIG. 1. Experimental realization. (a) Schematic of the in-house polarizer device. The sample (red) is mounted on a sample stick, which allows it to be moved between a MW cavity and an NMR coil inside a magnetic field at cryogenic temperatures. The laser is coupled to the system via an optical fiber. (b) Level scheme of pentacene (electron spin) and naphthalene-based protons (nuclear spins), including the effect of laser excitation (green) and natural decay (blue). Spin diffusion to external nuclear spins [17] is indicated. (c) 30 s of hyperpolarization show a clear signal enhancement compared with a 1-h thermal buildup; the thermal signal is scaled by a factor of 50 to emphasize its faint polarization peaks. (d) Schematic of the pulse sequence, consisting of a laser pulse for electron spin initialization and a MW pulse (of variable frequency) for polarization transfer to the nuclear spins. This basic block is repeated with a repetition rate of 1 kHz (i.e., 30 000 repetitions are performed in 30 s). After the polarization, the sample is shuttled into the NMR coil, where the magnetization is measured. An integral over the detected proton polarization is passed to REDCRAB, which provides the shape of the next MW pulse.

experimental setup is given in Sec. III B. The polarization results are introduced in Sec. IV A, and a description of the ARISE protocol is given Sec. IV B. The model used in the simulation is introduced in Sec. V, and details of the simulation are given in Sec. V A. In Sec. VI the results of the paper are put into context.

II. BACKGROUND

A. Pentacene-doped naphthalene crystals as a target

The system of naphthalene doped with pentacene, shown in Fig. 1(b), exhibits unique properties. In its ground state, the electron spin is in a singlet state, and therefore the host crystal is free of paramagnetic defects. Consequently, proton relaxation times of 50 h and above have been demonstrated at 77 K and 0.5 T [13].

In its metastable triplet state, the pentacene molecule exhibits a highly polarized electron spin with favorable lifetimes. Together with surrounding nuclear spins, this forms a central spin system that resembles other well-known systems such as nitrogen vacancy (NV) centers in diamond or phosphorus in silicon. This quantum resource for DNP leads to record values of 80% proton polarization [14], which amounts to a polarized proton concentration of 50 M. Exemplary applications of these nuclear-spin-polarized crystals are portable

neutron spin filters in neutron scattering experiments [13,15] and polarization agents for NMR spectroscopy [12,16].

Under typical operating conditions (e.g., high magnetic field), electron and nuclear spins are mutually off-resonant, prohibiting direct polarization transfer. Advanced spin control methods, such as DNP, can be used to transfer polarization. Real-world experimental constraints such as material quality, field inhomogeneities, and limited power and bandwidth commonly impair the ideal performance of existing DNP methods. Under such constraints, the maximum achievable polarization is reduced, and the time to reach a certain polarization increases.

B. Existing DNP strategies

In the case where the heterogeneity among spins is sufficiently small, they are all equally well controllable. As a result, techniques such as nuclear orientation via electron-spin locking (NOVEL) [18,19] can be employed to transfer polarization. As the environmental complexity and inhomogeneity increase, other techniques are needed. Transferring polarization while counteracting a broad electron spin resonance (ESR) is done with the so-called "integrated solid effect" (ISE) [20,21]: After the electron spin initialization, either a linear magnetic field sweep is performed, while the sample is driven by a constant microwave (MW) field B_1, or a

linear MW frequency sweep is performed at a static magnetic field. The ISE method is notable for both its simplicity and its robustness and has been shown to reach up to 80% total nuclear polarization in naphthalene under optimized conditions (e.g., liquid He cooling, sample quality) [14]. It has also been applied to NV centers in diamond at room temperature [11,22–24]. While optimizing DNP sequences on a model, i.e., performing open-loop quantum optimal control, is one method to recover some of their performance [25–27], another is to employ closed-loop QOC by allowing an algorithm to directly control the experiment [shown in Fig. 1(d)] [28–32]. The latter approach is particularly appealing when the experimental setting is very complex or impossible to accurately model. Due to the complex molecular environment, coupled with experimental constraints, the system's true transfer function is obscured, making accurate simulation difficult.

C. Quantum optimal control

Many advances in quantum technology were only possible due to the design of sophisticated control strategies using methods of QOC [28–32]. Established methods of QOC include gradient-based algorithms such as gradient ascent pulse engineering (GRAPE) [33,34], the Krotov algorithm [35,36], or gradient-based algorithms based on automatic differentiation [37], as well as algorithms based on an expansion of the control pulse into a truncated basis such as the dressed chopped random basis (dCRAB) algorithm [32,38,39], typically coupled with direct search maximization algorithms. This pulse expansion ansatz can also be combined with the gradient approach [40–42]. The dCRAB algorithm is readily applicable to closed-loop control as it can be integrated directly with an experiment, allowing the user to treat the system as a black box. For this purpose, the dCRAB algorithm was implemented in the QOC software packages Remote-dCRAB (REDCRAB) [43–46] and its open-source version, Quantum Optimal Control Suite (QUOCS) [47]. Recently, REDCRAB enabled automatic calibration of quantum gates [45] and robust sensing operations [48] with NV centers in diamond, optimization of Bose-Einstein condensate (BEC) creation in ultracold atoms [46], and the creation of a 20-atom Schrödinger cat state with Rydberg atoms in an optical lattice [49].

III. METHODS

A naphthalene crystal doped with pentacene-d_{14} grown in-house provides the electron spin system used as the polarization target. The crystal is placed in a magnetic field of 230 mT at around 130 K. This temperature is chosen because this is the limit of the polarizer. A series of laser pulses initialize the pentacene molecules into their metastable spin-polarized triplet state $\mathcal{T}_2$ [see Fig. 1(a)] via the singlet state $\mathcal{S}_1$, from which it decays to the lower $\mathcal{T}_1$ triplet via intersystem crossing (ISC) [50]. Depending on the occupation of the $\mathcal{T}_1$ states, the pentacene returns to its ground state $\mathcal{S}_0$ after 80–180 μs. During this intermediate time, a MW DNP sequence transfers electron spin polarization to the densely packed proximal proton spins. Strong dipolar coupling among protons distributes polarization throughout the entire crystal
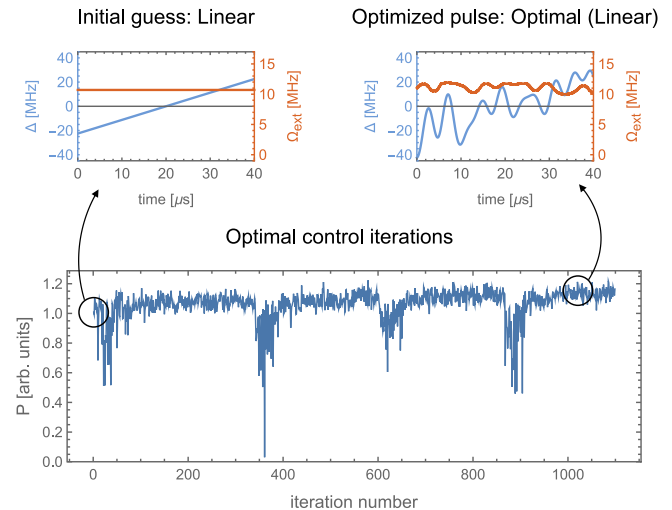

FIG. 2. Optimization procedure. Comparison between the linear sweep pulse (top left) and the pulse after optimization (top right). The MW amplitudes are shown in orange, and the detuning from cavity resonance is shown in blue, representing the control pulses, which are shaped during the optimization. Bottom: The change in the final polarization after the pulse over different sub- and superiterations during the optimization.

via spin diffusion. The macroscopic proton polarization is measured via NMR spectroscopy after a 30-s buildup [see Fig. 1(c)].

Starting from an external linear sweep (similar to ISE), and altering the amplitude and phase of the MW pulse using REDCRAB, this polarization is optimized (for more details, see Sec. IV B). The optimization starting from a linear sweep is shown in Fig. 2. Closed-loop QOC implicitly accounts for all experimental conditions influencing the transfer from optically initialized pentacene spins to macroscopic polarization. These could be, for example, the different lifetimes in the metastable state for different electron spin states or variations of the pentacene lifetimes throughout the crystal which might impact the final polarization.

Another potential source of uncertainty could be the strong variation of couplings between the electron and surrounding proton spins or the distribution of polarization via spin diffusion during and after the MW DNP sequence. Fluctuations in the experimental setup might also play a role, as bandwidth limitations of microwave equipment, spatial and spectral MW field variation inside the MW resonator, and spatial variation of laser intensity can also impact the efficiency. Additionally, it is challenging to control the amplitude of the MW field while its frequency is scanned across the resonance. Black-box (closed-loop) QOC does not directly incorporate variations in these parameters, whose role in polarization transfer is not understood; however, if they play a role, it can be captured by such an optimization. Importantly, some of these influences are very hard to predict theoretically.

A. Measurement technique

The crystal grown in-house is cleaved along the *ab* crystallographic plane and mounted on a sample holder [see

Fig. 1(a)] oriented along the *b* crystallographic axis. The sample holder is then attached to a motorized stage, enabling it to be shuttled into the MW cavity, where it is cooled to 130 K. Optically detected magnetic resonance (ODMR) can be observed in pentacene-doped naphthalene crystals, where the triplet state is created using a 556-nm laser pulse. By observing the fluorescence of the crystal under constant MW illumination, while changing the magnetic field, the electron spin resonance of pentacene can be found. The high-field transition of the pentacene triplet is used for both alignment and polarization. The crystal is then aligned by monitoring the ODMR spectrum while the sample is rotated; the best alignment is found when the resonance field is maximized. Rabi oscillations are observed with a maximum Rabi frequency of 19.3 MHz, by varying the duration of a resonant MW pulse.

B. Experimental realization

The experimental results are obtained in an in-house polarizer device, shown in Fig. 1(a), consisting of an optically accessible MW cavity inside an electromagnet operating at fields up to 800 mT. The experimental sequence used to hyperpolarize the sample is shown in Fig. 1(d). Within the MW cavity, photoexcited triplet states are created using a 556-nm pulsed laser with a repetition rate of 1 kHz delivering 0.35 mJ optical power in a 600-ns laser pulse every 1 ms and setting the timing of experiments. The spin state is then manipulated using a MW pulse in between laser pulses. Sophisticated pulse shapes can be sampled and uploaded to an arbitrary waveform generator (AWG) using the experiment control software QUDI [51]. The sample is attached to a holder that allows it to be shuttled into an NMR coil, which is located next to the MW cavity. Here, an NMR spectrometer (Magritek Kea^2) is used to read out the polarization of the proton spins using a 1Pulse measurement. This round trip takes approximately 40 s from the pulse engineered by the REDCRAB software to the NMR measurement, and the optimizations typically ran for 12 h. Integrating over the peak of the resulting NMR spectrum provides a relative estimate of the proton polarization. The REDCRAB algorithm is fed with this integrated signal and its estimated uncertainty to produce the next guess pulse.

An optional 532-nm continuous wave laser additionally allows the readout of the pentacene's electronic spin state optically; it is not used during closed-loop optimizations, but during the pentacene spin characterization experiments. Cooling of the sample is provided by a nitrogen gas flow system, which allows precise control of the temperature from 130 K to above room temperature; as previously mentioned the experiments are carried out at this lower limit.

IV. RESULTS

A. Polarization buildup

The optimization directly adjusts the pulse phase for experimental convenience, but as the detuning modulation Δ contains the same information and connects directly to the system dynamics, it is displayed in Fig. 3 instead. The first row of Fig. 3 shows the detuning modulation Δ as a function of time during the pulse. In the second row, the *y* axis shows the amplitude Ω during the pulse for both the externally ap-

plied field and the internal cavity field. The Hartmann-Hahn resonance [52], shown in orange, is calculated using the time-dependent detuning assuming the target spin is a proton. In the third row of Fig. 3, experimental data and simulation are compared, showing how the polarization builds up during the pulse.

The first initial guess pulse is an ISE-like linear sweep whose parameters (amplitude, sweep rate, and duration) had already been manually tuned in the experimental setup. The externally applied amplitude is kept constant, while the frequency is swept across the resonance. This pulse serves as the benchmark against which the optimized pulses are compared both in the experiment and in the simulation.

During the experiment, the polarization plateaus at the center of the pulse before continuing to rise in the second half of the pulse. The simulation results contain the same features. However, the plateau is shorter and the initial rise is slightly delayed compared with the experimental data. These differences might be caused by the lack of a full analytical model that extends the existing description of the cavity with distortions due to electronics and other components of the setup. It should be noted that polarization plateaus occur in the simulated results across all pulses when the detuning is above the resonance condition.

The optimization of this guess results in the pulse labeled "optimal (linear)," which shows a relative polarization improvement of approximately 19%. The evolution of the figure of merit (FoM) during the search for an optimized pulse and the comparison between the initial and the optimized version are shown in Fig. 2.

The "optimal (linear)" pulse transfers the majority of its polarization during the first 10 μs. It is notable that the detuning is oscillating during that time, and it crosses the cavity resonance several times. The algorithm slows the sweep down as the detuning approaches the resonance. Both features appear in multiple optimization outcomes. Arguably, if some electron population is left untransferred, subsequent sweeps through the resonance in both directions (from positive to negative detuning and back) can serve as additional opportunities for the polarization of more weakly coupled nuclear spins.

The relative speedup of the polarization transfer during this pulse is visible in both the simulation and the experiment. However, a divergence between the measurement and the simulation arises in the latter part of the pulse. This could be explained by the very fast oscillations in cavity field amplitude, which are not captured in full detail in the simulation, due to the unknown transfer function of the setup's electronics.

After analyzing the effect of the amplitude and phase of the pulse independently (see Appendix A for more details), the MW amplitude is kept constant in later optimizations. To further explore the idea that repeated sweeps through the resonance are beneficial, pulses with phase oscillations that use a range of frequencies and pulse durations are tested; see Appendix B for more details. The "sinusoidal" pulse shown in the third column of Fig. 3 is guessed in this manner. It outperforms the linear sweep by approximately 14%. The "sinusoidal" protocol in Fig. 3 then becomes the new guess pulse for the optimal control algorithm. After adding more frequency components, REDCRAB obtains the "optimal
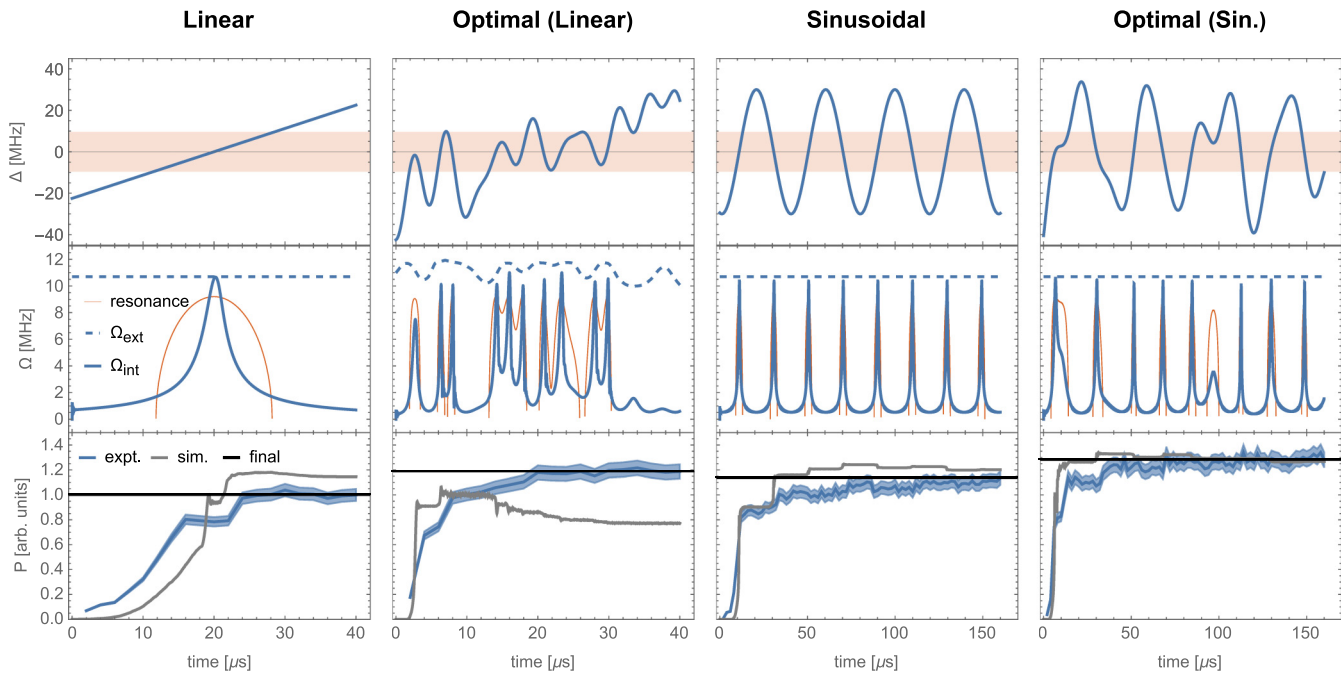
FIG. 3. Implementation of a selection of polarization pulses. From left to right, the figure presents the following MW pulse schemes on the resonator: The externally applied linear sweep, a linear sweep-based QOC-generated pulse, a sinusoidal sweep of the detuning, and a corresponding QOC-generated pulse. The first row gives the detuning applied by the drive with respect to time. The orange area comprises the window in which the Hartmann-Hahn resonance condition lies ($\Delta^2 = \omega_{0I}^2 - \Omega^2$). The second row shows the Rabi frequency as applied externally (dashed line), the field inside the cavity (solid blue line), and the resonance condition for the given detuning (thin orange line). The last row shows how the polarization builds up over the course of the pulse. Experimental values (expt.) are shown in blue, and theoretical values (sim. for simulation) are shown in gray. To make the comparison between the panels easier, we inserted a solid black line representing each pulse's final polarization. Optimal (Sin.), Optimal (sinusoidal).

(sinusoidal)" pulse. It outperforms all other pulses in both final polarization (approximately 28% higher with respect to the linear sweep for the short-buildup measurement) and polarization rate in our setup. When the pulse is significantly detuned from the resonance, as in the first 5 μs, the energy gap between the spins is large, and so very little polarization can be transferred. As this gap closes, the nuclei are more likely to be polarized, and the pulse slows down to allow for an extended transfer period. The detuning "slow-down" was re-created with an analytical polynomial function. (For details, see Appendix C.) The resulting "fitted optimal" pulse largely retains the polarization capability of the optimized pulse. The comparable efficiency corroborates that the "slowdown" feature contributes to the substantial polarization buildup during the first 30 μs. This behavior is reminiscent of optimal adiabatic passages with Landau-Zener protocols and optimal controlled crossings of quantum phase transitions. Both have been investigated in different theoretical and experimental scenarios [53–57] providing a basis for further exploration.

The simulated polarization of both the "sinusoidal" pulse and the "optimal (sinusoidal)" pulse matches the experimental data closely. Again, the initial step-plateau-step shape of the "sinusoidal" pulse is reduced after optimization. Almost all the performance gained by optimizing the pulses arises from the behavior during the first 40–50 μs of the pulse. This is on a timescale similar to that of the electron's decay to the singlet state. In the simulation, the polarization of the longer pulses

slowly decreases after approximately 80 μs. This was not seen in the experiment, most likely due to spin diffusion. Many weakly coupled nuclear spins could lead to a slow distribution of polarization away from the electron spin. Spin diffusion is expected on a timescale of approximately 100 μs according to calculations of the dipolar interaction strength between the protons [17].

The key result of the paper is shown in Fig. 4, where the REDCRAB-optimized "optimal (sinusoidal)" pulse demonstrates two clear improvements over the linear sweep. Firstly, the magnitude of polarization increases by 26% when using the optimized pulse. Secondly, the optimized pulse reaches, in only 3.35 h, the same polarization that the linear sweep approach obtains after 9 h of continuously repeating the protocol, making it a factor of 2.6 faster. These times correspond to $\sim 98\%$ of the maximum polarization of the linear sweep, which is within the error margin of the polarization measurements. The rate of polarization buildup is 15% faster compared with the linear sweep. This allows for more than doubling the number of polarized crystals in a given time. Previously, crystals were left to polarize overnight to reach sufficiently high polarization. Using the optimal protocol, it is now possible, in the current experimental setup, to polarize several crystals per day. Due to its increased performance, the "optimal (sinusoidal)" pulse was also applied as the hyperpolarization method of choice by Eichhorn *et al.* [12]. In that paper, a bulk crystal polarization of 25% is achieved using the optimized pulse.
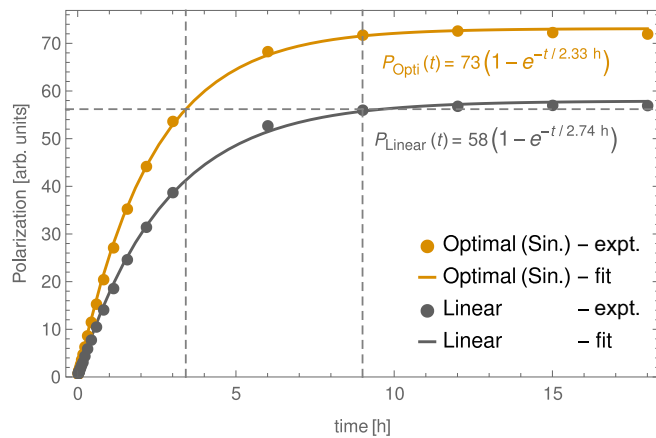
FIG. 4. Long-term polarization buildup: Comparing the polarization buildup using the optimal settings for the linear sweep and the REDCRAB-optimized pulse, shown in Fig. 3. Using closed-loop optimal control, a higher final polarization is reached in a shorter buildup time before saturation. The vertical dashed lines mark the times at which the polarization reaches 98% of the maximum polarization of the linear sweep pulse. This level is reached in 3.35 h using the optimized pulse, in contrast to 9 h with the linear sweep. The formulas placed in the figure correspond to the exponential fits, P_{Opti} and P_{Linear}, of the polarization buildup during the optimized pulse and the linear sweep, respectively.

The saturation of the polarization at this higher level is likely due to an equilibrium being reached between the polarizing sequence and the competing T_1 decay process of the nuclear spins [17]. The lifetime of the nuclear states is measured to be approximately 3–4 h under laser illumination, considering the specific values for the magnetic field B_0 and temperature. In this case, it is limited due to the laser illumination and MW fields causing, for example, additional heating. While this is the limit for the lifetime during polarization transfer, the polarization can be stored in the sample afterwards for much longer. Lifetimes between 50 h [12] and 800 h [13] have been reported for similar crystals at different temperatures and magnetic fields.

Additionally, by examining the shape of the optimized pulse and fitting its main features, a simplified analytical function is obtained describing the pulse (shown in Appendix C), labeled "fitted optimal". This retains most of the enhanced performance of the optimized sweep.

B. ARISE

Generalizing the steps taken to achieve the results of the previous section, the autonomously optimized repeated linear sweep (ARISE) procedure is introduced. Each step provides a recipe for finding a good initial guess for the proceeding optimization. While this should be unimportant for an infinite-dimensionally parametrized optimization without limits and infinite measurement precision, in practice those restrictions apply, leading the algorithm to local instead of global optima. Despite the dCRAB algorithm's approach allowing it to escape local minima under certain circumstances, the optimization time is also drastically reduced if the initial guess is chosen carefully [32]. The protocol consists of three steps:

(i) Tune the linear sweep. Do a parameter search for the sweep range Δ_{max} and duration t_{Linear} producing the most efficient polarization transfer.

(ii) Construct a multisweep. Set up a protocol which sweeps the detuning repeatedly between Δ_{max} and $-\Delta_{\mathrm{max}}$ for N_{osc} times with a period τ. Do a parameter search for N_{osc} and τ, starting from $\tau = t_{\mathrm{Linear}}$.

(iii) Apply quantum optimal control. Search the full function space of the detuning $\Delta(t)$ using an optimal control algorithm. The initial guess is provided by the multisweep protocol from the previous step.

In this paper, steps (i) and (ii) are accomplished through a simple parameter sweep. During step (ii), the detuning is swept with the function $-\Delta_{\mathrm{max}} \cos(2\pi t/\tau)$; however, this could be replaced by linear sweeps. As the setup requires the pulse phase $\varphi_{\mathrm{ext}}(t)$ as an input, all detunings are translated to phase modulations (see Sec. V). In general, experimental feedback determines the best solution for the respective step. Here, it took the form of the proton NMR signal after 30 000 repetitions of the sequence. The third step is implemented using the REDCRAB software, which suggests different shapes for the phase of the pulse (see Appendix H).

V. THEORY

The spin system is modeled as an electron spin coupled to three nuclear spins. Both the electron and nuclear spins are considered to be spin-$\frac{1}{2}$ particles. A strong, constant magnetic field $\boldsymbol{B}_0 = B_0\hat{z}$ is aligned along the long axis of the pentacene molecule, representing the z axis. The total spin Hamiltonian of the electron can be written as

$$H_{\mathrm{el}} = \frac{\hbar}{2}\omega_{0S}\sigma_z + \frac{\hbar^2}{4}\left[D\left(\sigma_z^2 - \frac{1}{3}\boldsymbol{\sigma}(\boldsymbol{\sigma}+1)\right) \right.$$
$$\left. + E\left(\sigma_x^2 - \sigma_y^2\right) \right], \tag{1}$$

where $\boldsymbol{\sigma} = \{\sigma_x, \sigma_y, \sigma_z\}$ are the Pauli matrices. The Zeeman interaction is described by $\omega_{0S} = -\gamma_S B_0$, where γ_S is the electron spin's gyromagnetic ratio. The factors D and E correspond to the zero-field splitting [50,58]. The exact transition frequency is determined experimentally, and the magnetic field is aligned such that the splitting is symmetric.

As shown in Fig. 1(b) the electron spin of the pentacene molecule is excited to the $\mathcal{S}_1$ state with a short laser pulse. From there it decays to the triplet states $\mathcal{T}_2$ and subsequently $\mathcal{T}_1$ via intersystem crossing (ISC) [50]. $\mathcal{T}_1$ then couples to the nuclear spins in the vicinity of the molecule. The three states of the triplet correspond to spin quantum numbers $m_s = 0$ and $m_s = \pm 1$. An external magnetic field induces a Zeeman splitting of the $m_s = \pm 1$ levels, allowing for a two-level approximation. As the pentacene is deuterated, the resonances of the pentacene's own nuclear spins are shifted far enough from the other protons in the crystal that they can be neglected. The electron spin is assumed to have its origin at the center of the pentacene molecule. To extract the parallel and perpendicular dipolar coupling to the pentacene's electron spin, 574 protons of the nearest naphthalene molecules contained

in the $3 \times 3 \times 3$ unit cells around the pentacene molecule are modeled.

The driving field has a carrier frequency which is resonant with the electron spin $\omega_{\mathrm{res}} = D - \omega_{0S}$. Its amplitude $\Omega_{\mathrm{ext}}(t)$ and phase $\varphi_{\mathrm{ext}}(t)$ are modulated to control the system. It is then transformed into the field inside the cavity Ω_{int} [the details are given below in Eq. (4)].

Coupling between the electron and nuclear spins is described by the hyperfine interaction tensor $\mathbf{A}^i$ with the nuclear spin indices $i = \{1, 2, 3\}$. A detuning Δ_{es} is introduced, describing the deviation of the field inside the cavity from the electron resonance frequency. In the rotating frame of the MW, and after applying the rotating wave approximation, the Hamiltonian is given by [59]

$$
H = \hbar \Bigg(\mathrm{Re}[\Omega_{\mathrm{int}}(t)]S_x + \mathrm{Im}[\Omega_{\mathrm{int}}(t)]S_y + \Delta_{\mathrm{es}} S_z
$$
$$
+ \omega_{\mathrm{L}} \sum_{i=1}^{3} I_z^i + \sum_{i=1}^{3} \mathbf{S} \cdot \mathbf{A}^i \cdot \mathbf{I}^i \Bigg),
\tag{2}
$$

where $\mathbf{S} = \{S_x, S_y, S_z\}$ with $S_k = \frac{1}{2}\sigma_k \otimes \mathbb{1} \otimes \mathbb{1} \otimes \mathbb{1}$ ($k \in \{x, y, z\}$) are the electron's spin operators. $\mathbf{I}^i$ and I_k^i are the equivalent operators for the nuclear spin with index i, Ω_{int} is the complex, time-dependent field inside the cavity, and $\omega_{\mathrm{L}} \approx 9.2$ MHz corresponds to the Larmor frequency of the nuclei. The voltage signal, which is fed into the AWG, is given by

$$
V_{\mathrm{ext}} = V(t) \cos\left((\omega_{\mathrm{res}} + \Delta_{\mathrm{cs}})t + \varphi_{\mathrm{ext}}(t)\right).
\tag{3}
$$

The conversion between $V(t)$ and $\Omega_{\mathrm{ext}}(t)$ is determined directly from experimental data. The phase modulation $\varphi_{\mathrm{ext}}(t)$ can be translated into the drive detuning $\Delta(t) = \dot{\varphi}_{\mathrm{ext}}(t)$.

The effect of the cavity on the external driving field is characterized by the cavity response factor γ_{cav} and given by the differential equation

$$
\frac{\partial}{\partial t}\Omega_{\mathrm{int}}(t) = \gamma_{\mathrm{cav}}(\Omega_{\mathrm{ext}}(t) \cdot e^{-i\varphi_{\mathrm{ext}}(t)} - \Omega_{\mathrm{int}}(t))
$$
$$
- i\Delta_{\mathrm{cs}}\Omega_{\mathrm{int}},
\tag{4}
$$

where Δ_{cs} describes the constant detuning of the cavity from the resonance of the electron spin transition frequency [60].

In the secular approximation [61], only the dominant coupling terms along z are kept, giving

$$
\mathbf{S} \cdot \mathbf{A}^i \cdot \mathbf{I}^i \approx S_z \cdot \left(A_{zx}^i I_x^i + A_{zy}^i I_y^i + A_{zz}^i I_z^i\right).
\tag{5}
$$

They are calculated for the respective position of the nucleus in the crystal structure by considering a purely dipolar interaction [62].

The static detuning values Δ_{es} for the Hamiltonian shown in Eq. (2) are drawn from a normal distribution with a full width at half maximum (FWHM) of 10 MHz to mimic additional frequency shifts due to magnetic field inhomogeneities and other impurities.

The system description includes the dephasing of the electron spin via a Lindblad operator $R_1 = \sqrt{\frac{\Gamma_{\mathrm{el}}}{2}} S_z$, where Γ_{el} is the dephasing rate [63]. The only electron states that interact with surrounding nuclei are the $|0\rangle$ and $|1\rangle$ states in the $\mathcal{T}_1$ triplet (see Fig. 1). To account for the decay from $\mathcal{T}_1$ to $\mathcal{S}_0$,

the model includes a shelf state, which does not interact with the drive. It is only coupled via the loss rates $\Gamma_{\mathrm{loss},0}$ and $\Gamma_{\mathrm{loss},1}$ from the respective triplet states. The corresponding Lindbladians are given by $R_2 = \sqrt{\Gamma_{\mathrm{loss},0}}\, \sigma_{-,0}$ and $R_3 = \sqrt{\Gamma_{\mathrm{loss},1}}\, \sigma_{-,1}$ with $\sigma_{-,0} = |s\rangle\langle 0|$ and $\sigma_{-,1} = |s\rangle\langle 1|$.

The evolution of the density matrix is then solved using the Lindblad master equation

$$
\dot{\rho} = -\frac{i}{\hbar}[H, \rho] + \sum_{j=1,2,3} \left(R_j \rho R_j^\dagger - \frac{1}{2}R_j^\dagger R_j \rho - \frac{1}{2}\rho R_j^\dagger R_j\right),
\tag{6}
$$

where ρ is the density matrix of the system.

A. Simulation

The solutions to the differential equations in Eqs. (6) and (4) are calculated numerically using DIFFERENTIALEQUATIONS.JL [64] and other JULIA packages [65–78]. To obtain a realistic polarization buildup, Eq. (6) is solved for and averaged over 1000 instances. For each instance, three random but distinct nuclei are picked from the 30 most strongly coupled nuclei, and the detuning Δ_{es} is sampled from a Gaussian distribution. This way, mechanisms which are neglected in the common weighted-sum single-nucleus approximation are captured. Examples include the repolarization of the electron spin through partially polarized nuclei or the redistribution of polarization from one nucleus to another. The mean over many runs with different coupling combinations takes into account the variety of couplings in the system with reasonable computational resources.

The cavity response γ_{cav} is determined by repeatedly applying constant external drive fields with different cavity detunings Δ_{cs}, obtaining a photon count that corresponds to the electron state.

B_0 is adjusted such that the spin always stays resonant with the drive frequency. Oscillations are recorded for times up to $0.6\,\mu$s from the start of the drive pulse. The detuning is swept through a range of ± 25 MHz around the resonance. The maximum of the Fourier transform of the photon count then corresponds to the Rabi frequency Ω for a detuning Δ_{cs}. The cavity dynamics are complex, leading to a response similar to the example shown at the top right of Fig. 5. These measurements are modeled for an electron spin inside a cavity with a response factor γ_{cav} between 5 and 14 MHz (range suggested by response time based on the measured Q factor of the resonator using a spectrum analyzer). The resulting Fourier transforms are compared with the experimental values. The comparison was done by calculating the overlap of the normalized measurement and simulation grids, as shown in Fig. 5. The minimum of the sum of the absolute difference between each grid point of the measurement and simulation data is obtained by a Gaussian fit resulting in $\gamma_{\mathrm{cav}} = 9.24$ MHz.

The values for the decoherence rate, Γ_{el}, of the electron spin and the loss rates to the shelf state, $\Gamma_{\mathrm{loss},0}$ and $\Gamma_{\mathrm{loss},-1}$, are found by performing a Hahn echo measurement and state-dependent lifetime measurements. For the dephasing time of the electron, $1/\Gamma_{\mathrm{el}} = 10\,\mu$s is obtained, and the
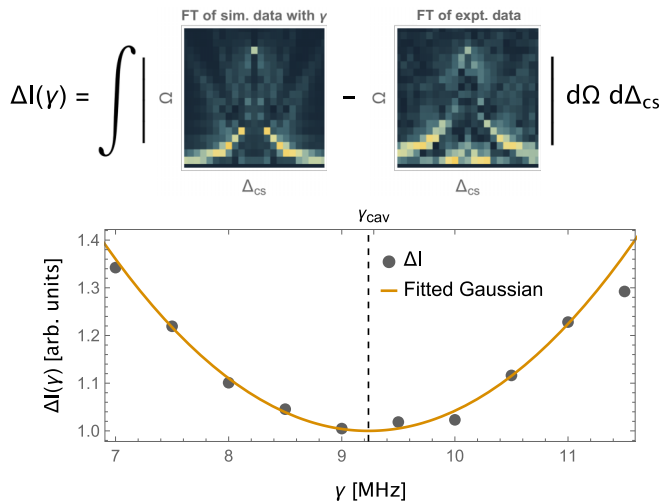
FIG. 5. Characterization of the setup via response factor γ. The agreement between experiment and simulation, ΔI, is calculated via the Fourier transform Ω of the driven Rabi signal for varying cavity detunings (top). The integral indicates the overlap of measured and simulated distributions, which is shown for different values of cavity response fed to the simulation in the bottom plot. The dashed black line indicates the minimum of the error in overlap between simulation end experiment at $\gamma_{\mathrm{cav}} = 9.24$ MHz (bottom). FT, Fourier transform.

triplet-state decay times are measured to be $1/\Gamma_{\mathrm{loss},0} = 80\ \mu$s and $1/\Gamma_{\mathrm{loss},-1} = 180\ \mu$s.

VI. DISCUSSION AND OUTLOOK

The use of closed-loop optimal control provides a strategy for improving hyperpolarized NMR signals in complex experimental setups despite the unknown transfer function. A concern often raised about numerically optimized sequences is that they lose generality and only apply to a specific setup or sample. In contrast, the "optimal (sinusoidal)" protocol has been successfully applied on different crystals with varying spin relaxation times across an extended period of time [12]. It is now the gold-standard pulse in the laboratory.

The combination of a 15% faster polarization rate and a 26% higher polarization level provides a factor of 2.6 reduction in the time taken to polarize crystals to within the margin of error of the previous method. As a result, multiple crystals can be polarized per day to be used in external hyperpolarization experiments [12]. Furthermore, these improvements lead to higher levels of polarization in a shorter time, resulting in an overall polarization within the crystal of about 25% [12]. Such strongly polarized crystals are necessary to transfer polarization to external nuclear spins. By operating under liquid helium conditions and with improved crystal quality, even higher values are anticipated [14]. Mimicking the features of the optimized pulse by fitting an analytical function to it (as shown in Appendix C) retains almost all the improved performance. It represents a good starting point not only for future optimization, but also for further investigations of the system dynamics.

A key feature of all the sequences that outperform the linear sweep is that they repeatedly sweep through the cavity resonance. Hence the sequences are given an extra opportunity to transfer polarization, suggesting that the first sweep leaves some electron polarization untransferred. The simulation shows that the first sweep primarily transfers to one of the most strongly coupled nuclear spins, while subsequent sweeps redistribute the polarization to a wider range of couplings. This type of dynamics can only be accounted for when multiple nuclear spins are considered or the optimization is done on a macroscopic system.

The ARISE protocol offers a starting point for future optimizations of DNP sequences using both open- and closed-loop protocols. Inherently flexible, the protocol is easily customized to fit any number of setups, including the complex molecular environment seen here.

In conclusion, the application of the ARISE protocol results in a 26% improvement in the polarization level and 15% faster polarization rate. Consequently, crystals were efficiently polarized to 25% bulk proton polarization. These crystals were then used as the polarization source for an external hyperpolarization experiment [12] which demonstrated strong transfer to external spins.

APPENDIX A: AMPLITUDE VERSUS PHASE VARIATION

To separate the respective effects of amplitude and phase modulation, these two parameters are investigated independently (Fig. 6). The first test was a basic linear sweep and the "optimal (linear)" pulse, where it was observed that the optimized pulse leads to higher polarization. To test only the optimized amplitude modulation, the optimized phase is reset to the initial guess while the phase modulation was kept ("optimal amplitude + linear phase"). Similarly, to test the optimized phase modulation, the amplitude is held constant, as in the linear sweep, and the optimized phase is applied ("linear amplitude + optimal phase").

By comparing those four pulses, it becomes clear that the amplitude modulation plays no role in the polarization transfer and only the pulses with optimally controlled phase modulation lead to enhanced polarization (highlighted in Fig. 6). Testing the phase of the optimized pulses with different constant MW amplitudes shows that using a higher MW amplitude always leads to better polarization transfer (see Fig. 8 in Appendix C).

APPENDIX B: SINE OSCILLATION FREQUENCY TESTS

Following the idea that subsequent sweeps through the resonance in alternating directions further enhance the
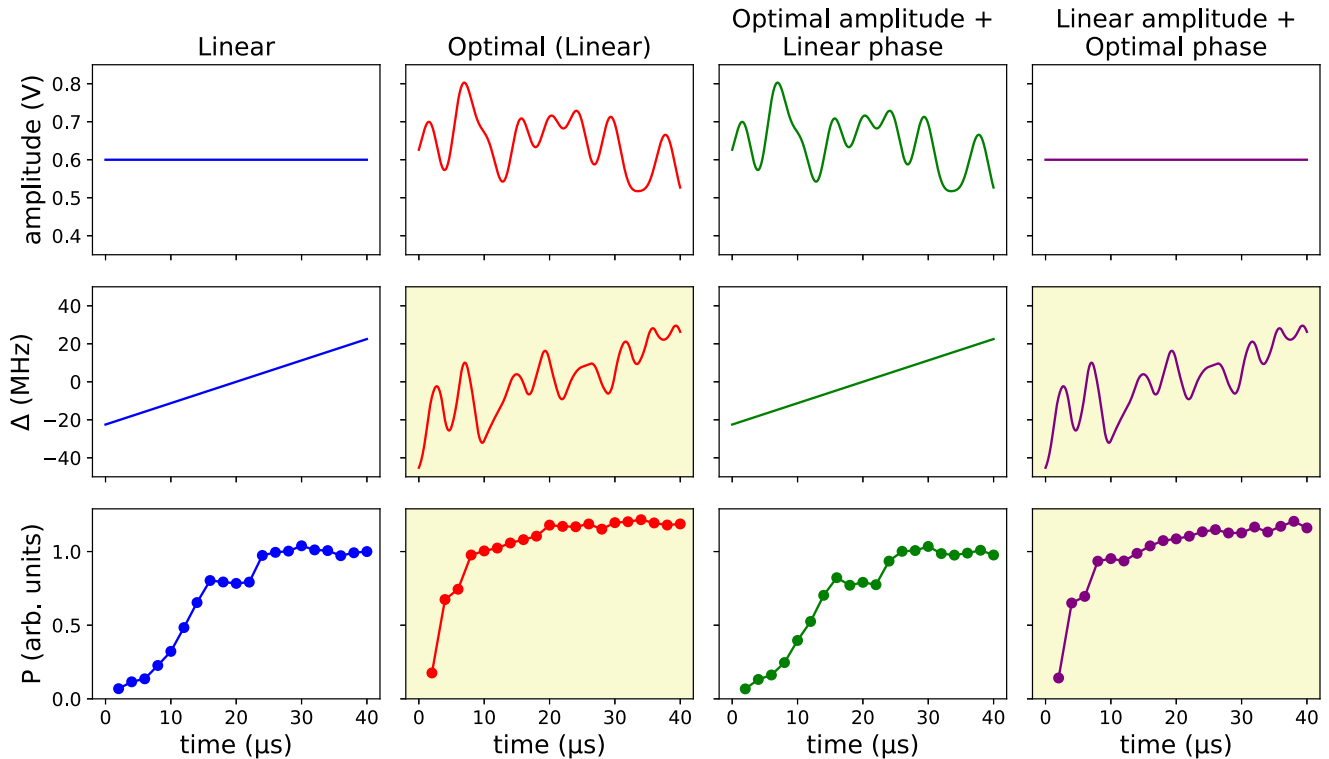
FIG. 6. Amplitude vs phase variations: Comparing the linear sweep ("linear") with the corresponding QOC-generated pulse ["optimal (linear)"], as well as combinations of both. In the third and fourth columns the amplitude array of one is combined with the phase array of the other ("optimal amplitude + linear phase" and "linear amplitude + optimal phase"). The increase in polarization over the optimization is caused solely by the changes in phase rather than amplitude (compare highlighted plots).

polarization, a sinusoidal pulse is tried. To find the optimal pulse, both the frequency of the oscillation and the number of resonance passages were varied. For better comparison, the length of a half oscillation is used as a parameter instead of the frequency, which means passing through the resonance once, similar to a basic ISE-like linear sweep [Fig. 7(a)]. The second parameter, which describes the passages through the resonance, is then given by the number of half oscillations [examples given in Fig. 7(c)].

In Fig. 7(b) the polarization for different parameter sets (length and number of half oscillation) is compared with the standard linear sweep (dashed line). Increasing the number of resonance passages leads to an increase in polarization for all lengths. While most of the applied pulses beat the standard linear pulse, a maximum polarization for a length of 20 μs and eight half oscillations was found [Fig. 7(d)]. This pulse was characterized in the main text and used a new starting point for the sinusoidal-based optimal control.

APPENDIX C: FITTED OPTIMIZED PULSE

The "fitted optimal" pulse shown on the right-hand side in Fig. 8 was designed by modeling the shoulder feature of the sinusoidal-based optimal control (OC) pulse resulting from closed-loop optimizations of the sinusoidally varying pulse in the detuning regime. Repeating mirrored polynomial functions emulate the slowdown of the detuning sweep around resonance. A variation of the externally applied voltage kept constant during the pulses displays an improvement of polar-

ization transfer for higher external drive amplitude. Except for the highest driving amplitudes, at the limit of the experimental capabilities, the fitted pulse is equal to or outperforms the pulse resulting from the closed-loop iterations. Therefore it serves as a good starting point for use in other, similar setups and further optimizations as well as theoretical and analytical transfer calculations and numerical simulations.

APPENDIX D: NAÏVE SWEEP CORRECTIONS

While a linear sweep is applied outside the cavity, the mentioned effects lead to a nonlinear sweep inside the cavity. However, the drive would appear faster when passing through the cavity resonance, compared with the part of the sweep far outside the resonance. Measuring the cavity linewidth and Q factor allows the calculation of the expected deviation from the linear sweep. Calculating an input function with modified amplitude that takes the cavity properties into account would be the first naïve approach to overcome this issue. Trying this did not, however, improve the polarization values.

APPENDIX E: COHERENCE MEASUREMENTS

The nuclear spin relaxation time T_1 and the electron spin coherence time T_2 were measured. For the nuclear spin relaxation time T_1 measured under experimental conditions (e.g., temperature, laser illumination), a value of around 223 min (Fig. 9, top) was recorded. For the coherence time of the electron spin, T_2, a standard Hahn-echo sequence [79] was
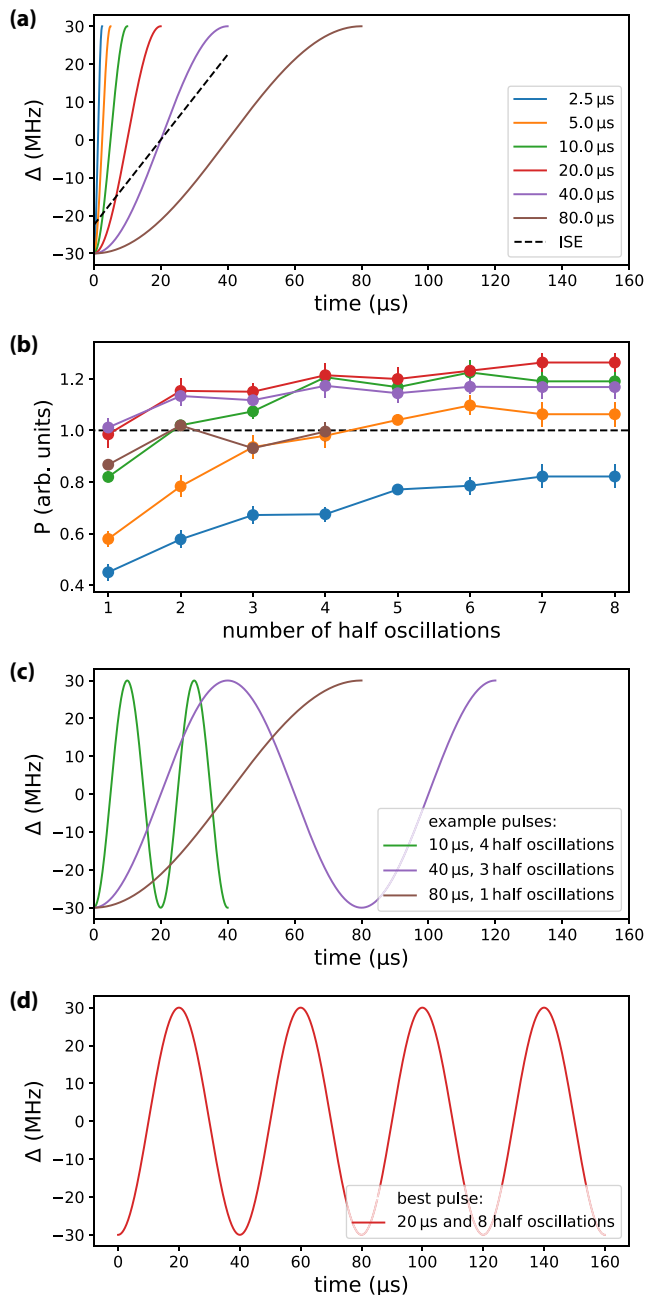
FIG. 7. Comparing different sinusoidal pulses. (a) Half oscillations with different frequencies comparable to different speeds of the ISE-like linear sequences. (b) For all six frequencies in (a), the polarization after up to eight half oscillations is measured and compared with the polarization after the linear sweep (dashed line). (c) Example pulses to visualize the idea of the measurement. (d) Sinusoidal pulse that gave the highest polarization.

used, and a value of around 9 μs was obtained (Fig. 9, bottom).

APPENDIX F: POLARIZATION BUILDUP

Polarization p in the crystal is built up by iteratively applying the basic polarization sequence many times (see Fig. 3 in the main text). The final polarization will be given at the
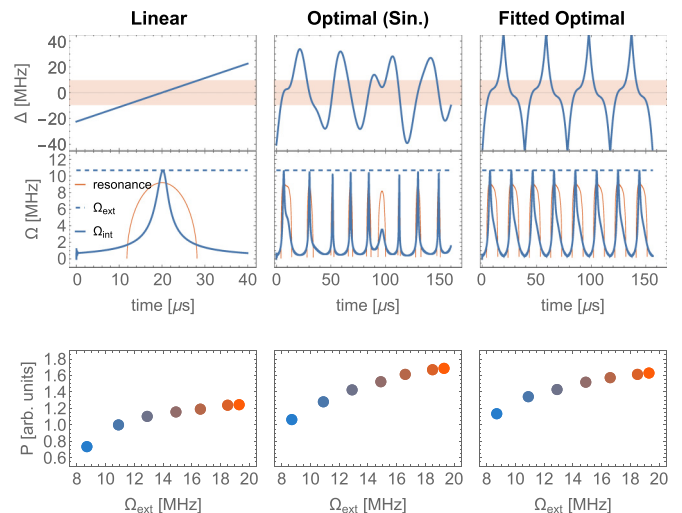

FIG. 8. Polarization performance of the linear sweep ("linear"), the QOC pulse generated from a sinusoidal initial guess ["optimal (sinusoidal)"], and its fit ("fitted optimal") for increasing constant drive amplitudes. Guided by the outcome of the optimal control algorithm, the first $\sim$20 μs of the "optimal (sinusoidal)" pulse are remodeled analytically by tuning polynomial functions to match the detuning's shoulder feature. Even for lower Rabi frequencies, the optimized pulses outperform the initial ISE-like linear approach.

equilibrium of two competing effects: Each time the basic sequence is applied, a fraction $\alpha(1-p)$ of the remaining unpolarized nuclear spins will be polarized, where α is the polarization power of the sequence. At the same time, the polarized nuclear spins decay at a constant rate γ.

$$\frac{dp}{dt} = \alpha(1-p) - \gamma p. \qquad (\text{F1})$$

Solving Eq. (F1) leads to the equation

$$p(t) = p_{\max}(1 - e^{-\tilde{\gamma}t}), \qquad (\text{F2})$$

where $p_{\max} = \alpha/(\gamma + \alpha)$ and the parameter $\tilde{\gamma} = \gamma + \alpha$ can be obtained from a fit to the data. From the polarization built up while applying a linear sweep, $\tilde{\gamma} \approx 0.0061$ min^{-1} and $p_{\max} \approx 14\,140$ arb. units are obtained. When applying the optimal sequence, $\tilde{\gamma} \approx 0.0071$ and $p_{\max} \approx 17\,850$ arb. units are obtained. An additional measurement, T_1, gives $1/\gamma \approx 223$ min (Fig. 9, top). This translates into estimates for the final polarization of $p_{\max} \approx (27.8 \pm 1.3)\%$ for the linear sweep and $p_{\max} \approx (35.1 \pm 1.7)\%$ for the optimal sequence. Note that the true value of γ is probably slightly larger than in the T_1 measurement due to the polarization pulse sequences. If, for example, $1/\gamma \approx 200$ min (or $1/\gamma \approx 180$ min) is considered, the polarization for the optimal sequence drops to $p_{\max} \approx (26.2 \pm 3.4)\%$ [or $p_{\max} \approx (16.5 \pm 5.2)\%$] and similarly for the linear sweep.

APPENDIX G: EFFECT OF THE NUMBER OF NUCLEI ON THE MODEL

Each electron spin is surrounded by a large number of protons, forming the nuclear spin bath. As only a limited number can be simulated at a time, subgroups of nuclei are considered
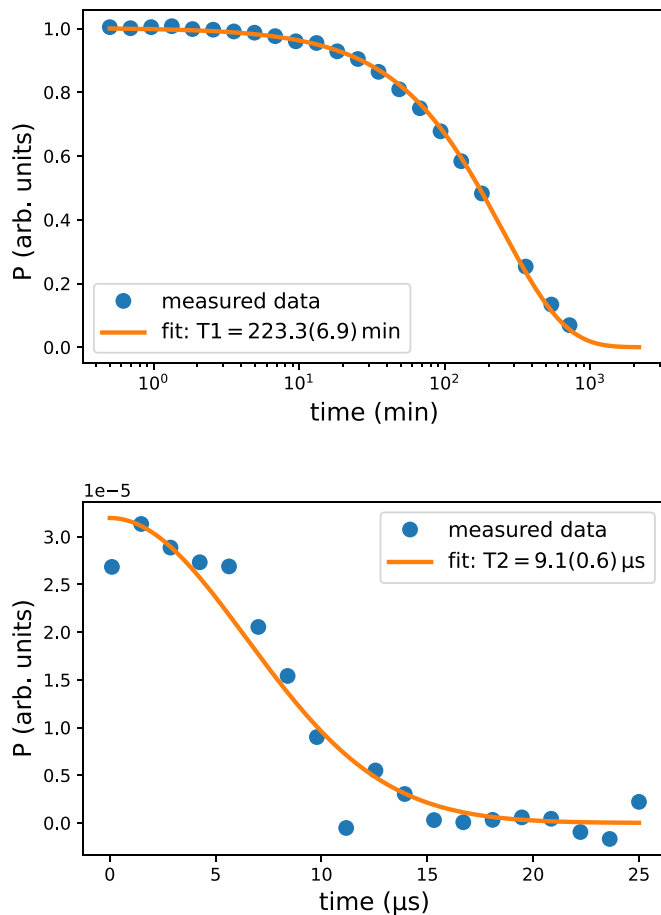
FIG. 9. Top: T_1 measurement of the nuclear spins under experimental conditions. Bottom: T_2 measurement of the electron spin via Hahn echo.

and averaged over. Fortunately, the molecular and crystallographic properties of the naphthalene-h_8 specimen doped with pentacene-d_{14} are well known. Hence the orthogonal (A_{zx}^i, A_{zy}^i) and parallel (A_{zz}^i) parts of the hyperfine tensor can be directly calculated [62] for the surrounding protons in the crystal. Instead of including the entire bath as a single effective nuclear spin [59], several nuclei are considered individually in the polarization dynamics. This step is necessary to reflect the effects caused by complex pulse shapes obtained by the optimization, as well as the distortion by the cavity. Since the pulses cross the resonance line multiple times and are repeated successively for polarization buildup, strongly coupled nuclei are usually polarized first but can be depolarized again so that excitation is transferred to other nuclear spins. Because the electron spin is reinitialized before each pulse application, each iteration can polarize different nuclei. Up to six nuclei were considered during the initial investigation. However, for the figures presented in this paper, the following combination of spins was used to keep computational resources within an acceptable range: The electron spin is coupled to three nuclear spins, where the hyperfine coupling values are randomly selected from the top 30 most strongly coupled protons. This simulation is repeated and averaged for 1000 sets using three different random nuclei in each run. This captures the

dynamics of multiple protons coupling to the electron at the same time, as well as the repetition of the transfer operation in the experiment.

APPENDIX H: QUANTUM OPTIMAL CONTROL

Optimal control methods aim to optimize a functional f by modifying time-dependent control functions $u_i(t)$. This functional is the figure of merit (FoM); it includes all the relevant information contributing to the quality of an operation. To simplify the optimization problem, the controls can be parametrized in terms of N_{be} basis functions $v_\ell(t)$ with corresponding parameters c_ℓ

$$u_i(t) = \sum_{\ell=1}^{N_{be}} c_\ell v_\ell(t). \tag{H1}$$

The FoM therefore depends on the coefficients of these basis functions:

$$\text{FoM}(u_i) = f(c_\ell, v_\ell, t). \tag{H2}$$

The solution to the problem is found using an iterative optimization algorithm, which takes in the FoM for a defined set of parameters and returns a new set of parameters. Closed-loop control involves the algorithm directly interacting with the experimental setup. Hence it automatically takes into account real-world imperfections. Specifics of the measurement technique can be found in Sec. III A of the main text. The algorithm improves the FoM by comparing the results from different iterations. It follows the direction of improvement, while exploring the parameter landscape and exploiting its features. An optimal set of controls is eventually obtained after a number of iterations and FoM evaluations.

Limiting the size of the parameter landscape reduces the number of experimental runs and hence the total optimization time. The dCRAB algorithm [32,38,39,80], in combination with the Nelder-Mead [81,82] simplex optimization algorithm, is a good choice for this. A small parameter space is created by randomly picking a number of basis functions, finding the optimal parameters for them, and then switching to a new basis set. An optimization in a single parameter space is called a superiteration. This allows the optimization to start afresh and continue, even if it temporarily gets stuck in a local optimum.

For the parametrization the Fourier basis is chosen, which provides a simple method to restrict the bandwidth of the controls by limiting their maximum oscillation frequency component through a capping of $\omega_{d,\ell}$ in

$$u(t) = \sum_{d=1}^{N_{SI}} \sum_{\ell=1}^{N_{be}} \left[A_{d,\ell}^{opt} \sin(\omega_{d,\ell} t) + B_{d,\ell}^{opt} \cos(\omega_{d,\ell} t) \right]. \tag{H3}$$

N_{be} represents the number of basis elements (i.e., the size of the parameter space in each superiteration), while N_{SI} corresponds to the number of superiterations. The parameter space of the optimization is spanned by $c_{d,\ell} = \{A_{d,\ell}^{opt}, B_{d,\ell}^{opt}\}$, while $\omega_{d,\ell}$ is randomly initialized with frequencies within a predefined interval for each superiteration defining the basis functions $v_{d,\ell} = \{\sin(\omega_{d,\ell} t), \cos(\omega_{d,\ell} t)\}$. Meanwhile, the length of the pulses is kept constant.

The combination of this limited search space for efficient closed-loop optimization together with the three-step ARISE protocol (see Sec. IV B in the main text) enables the encoding of a sufficient amount of information in the control pulse to substantially increase its performance [83].

---

[1] J. H. Ardenkjaer-Larsen, B. Fridlund, A. Gram, G. Hansson, L. Hansson, M. H. Lerche, R. Servin, M. Thaning, and K. Golman, Increase in signal-to-noise of >10,000 times in liquid-state NMR, Proc. Natl. Acad. Sci. USA **100**, 10158 (2003).

[2] Z. J. Wang, M. A. Ohliger, P. E. Z. Larson, J. W. Gordon, R. A. Bok, J. Slater, J. E. Villanueva-Meyer, C. P. Hess, J. Kurhanewicz, and D. B. Vigneron, Hyperpolarized ^{13}C MRI: State of the art and future directions, Radiology **291**, 273 (2019).

[3] K. Tateishi, M. Negoro, S. Nishida, A. Kagawa, Y. Morita, and M. Kitagawa, Room temperature hyperpolarization of nuclear spins in bulk, Proc. Natl. Acad. Sci. USA **111**, 7527 (2014).

[4] D. M. Lilburn, G. E. Pavlovskaya, and T. Meersmann, Perspectives of hyperpolarized noble gas MRI beyond ^{3}He, J. Magn. Reson. **229**, 173 (2013).

[5] M. S. Albert Jr, G. Cates, B. Driehuys, W. Happer, B. Saam, C. Springer Jr, and A. Wishnia, Biological magnetic resonance imaging using laser-polarized ^{129}Xe, Nature (London) **370**, 199 (1994).

[6] M. Auzinsh and R. Ferber, *Optical Polarization of Molecules* (Cambridge University Press, Cambridge, 2005).

[7] T. E. Lee, S. Gopalakrishnan, and M. D. Lukin, Unconventional Magnetism via Optical Pumping of Interacting Spin Systems, Phys. Rev. Lett. **110**, 257204 (2013).

[8] G. Liu, S.-H. Liou, N. Enkin, I. Tkach, and M. Bennati, Photo-induced radical polarization and liquid-state dynamic nuclear polarization using fullerene nitroxide derivatives, Phys. Chem. Chem. Phys. **19**, 31823 (2017).

[9] J. P. King, K. Jeong, C. C. Vassiliou, C. S. Shin, R. H. Page, C. E. Avalos, H.-J. Wang, and A. Pines, Room-temperature *in situ* nuclear spin hyperpolarization from optically pumped nitrogen vacancy centres in diamond, Nat. Commun. **6**, 8965 (2015).

[10] P. London, J. Scheuer, J.-M. Cai, I. Schwarz, A. Retzker, M. B. Plenio, M. Katagiri, T. Teraji, S. Koizumi, J. Isoya, R. Fischer, L. P. McGuinness, B. Naydenov, and F. Jelezko, Detecting and Polarizing Nuclear Spins with Double Resonance on a Single Electron Spin, Phys. Rev. Lett. **111**, 067601 (2013).

[11] J. Scheuer, I. Schwartz, Q. Chen, D. Schulze-Sünninghausen, P. Carl, P. Höfer, A. Retzker, H. Sumiya, J. Isoya, B. Luy, M. B. Plenio, B. Naydenov, and F. Jelezko, Optically induced dynamic nuclear spin polarisation in diamond, New J. Phys. **18**, 013040 (2016).

[12] T. R. Eichhorn, A. J. Parker, F. Josten, C. Müller, J. Scheuer, J. M. Steiner, M. Gierse, J. Handwerker, M. Keim, S. Lucas, M. U. Qureshi, A. Marshall, A. Salhov, Y. Quan, J. Binder, K. D. Jahnke, P. Neumann, S. Knecht, J. W. Blanchard, M. B. Plenio *et al.*, Hyperpolarized solution-state NMR spectroscopy with optically polarized crystals, J. Am. Chem. Soc. **144**, 2511 (2022).

[13] Y. Quan, B. van den Brandt, J. Kohlbrecher, W. Wenckebach, and P. Hautle, A transportable neutron spin filter, Nucl. Instrum. Methods Phys. Res., Sect. A **921**, 22 (2019).

[14] Y. Quan, N. Nekitic, B. van den Brandt, and P. Hautle, A novel broad-band neutron spin filter based on dynamically polarized protons using photo-excited triplet states, EPJ Web Conf. **219**, 10006 (2019).

[15] Y. Quan, B. van den Brandt, J. Kohlbrecher, and P. Hautle, Polarization analysis in small-angle neutron scattering with a transportable neutron spin filter based on polarized protons, J. Phys.: Conf. Ser. **1316**, 012010 (2019).

[16] H. Kouno, Y. Kawashima, K. Tateishi, T. Uesaka, N. Kimizuka, and N. Yanai, Nonpentacene polarizing agents with improved air stability for triplet dynamic nuclear polarization at room temperature, J. Phys. Chem. Lett. **10**, 2208 (2019).

[17] A. C. Pinon, J. Schlagnitweit, P. Berruyer, A. J. Rossini, M. Lelli, E. Socie, M. Tang, T. Pham, A. Lesage, S. Schantz, and L. Emsley, Measuring nano- to microstructures from relayed dynamic nuclear polarization NMR, J. Phys. Chem. C **121**, 15993 (2017).

[18] A. Henstra, P. Dirksen, J. Schmidt, and W. Wenckebach, Nuclear spin orientation via electron spin locking (NOVEL), J. Magn. Reson. (1969–1992) **77**, 389 (1988).

[19] H. Brunner, R. H. Fritsch, and K. H. Hausser, Notizen: Cross polarization in electron nuclear double resonance by satisfying the Hartmann-Hahn condition, Z. Naturforsch., A, Phys. Sci. **42**, 1456 (1987).

[20] A. Henstra, P. Dirksen, and W. Wenckebach, Enhanced dynamic nuclear polarization by the integrated solid effect, Phys. Lett. A **134**, 134 (1988).

[21] A. Henstra, T.-S. Lin, J. Schmidt, and W. Wenckebach, High dynamic nuclear polarization at room temperature, Chem. Phys. Lett. **165**, 6 (1990).

[22] K. Miyanishi, T. F. Segawa, K. Takeda, I. Ohki, S. Onoda, T. Ohshima, H. Abe, H. Takashima, S. Takeuchi, A. I. Shames, K. Morita, Y. Wang, F. T.-K. So, D. Terada, R. Igarashi, A. Kagawa, M. Kitagawa, N. Mizuochi, M. Shirakawa, and M. Negoro, Room-temperature hyperpolarization of poly-crystalline samples with optically polarized triplet electrons: Pentacene or nitrogen-vacancy center in diamond? Magn. Reson. **2**, 33 (2021).

[23] I. Schwartz, J. Scheuer, B. Tratzmiller, S. Müller, Q. Chen, I. Dhand, Z.-Y. Wang, C. Müller, B. Naydenov, F. Jelezko, and M. B. Plenio, Robust optical polarization of nuclear spin baths using Hamiltonian engineering of nitrogen-vacancy center quantum dynamics, Sci. Adv. **4**, eaat8978 (2018).

[24] Q. Chen, I. Schwarz, F. Jelezko, A. Retzker, and M. B. Plenio, Optical hyperpolarization of ^{13}C nuclear spins in nanodiamond ensembles, Phys. Rev. B **92**, 184420 (2015).

[25] H. Yuan, R. Zeier, N. Pomplun, S. J. Glaser, and N. Khaneja, Time-optimal polarization transfer from an electron spin to a nuclear spin, Phys. Rev. A **92**, 053414 (2015).

[26] N. Pomplun, B. Heitmann, N. Khaneja, and S. J. Glaser, Optimization of electron–nuclear polarization transfer, Appl. Magn. Reson. **34**, 331 (2008).

[27] N. Pomplun and S. J. Glaser, Exploring the limits of electron-nuclear polarization transfer efficiency in three-spin systems, Phys. Chem. Chem. Phys. **12**, 5791 (2010).

[28] C. Brif, R. Chakrabarti, and H. Rabitz, Control of quantum phenomena: Past, present and future, New J. Phys. **12**, 075008 (2010).

[29] S. J. Glaser, U. Boscain, T. Calarco, C. P. Koch, W. Köckenberger, R. Kosloff, I. Kuprov, B. Luy, S. Schirmer, T. Schulte-Herbrüggen, D. Sugny, and F. K. Wilhelm, Training Schrödinger's cat: Quantum optimal control, Eur. Phys. J. D **69**, 279 (2015).

[30] C. P. Koch, Controlling open quantum systems: Tools, achievements, and limitations, J. Phys.: Condens. Matter **28**, 213001 (2016).

[31] P. Rembold, N. Oshnik, M. M. Müller, S. Montangero, T. Calarco, and E. Neu, Introduction to quantum optimal control for quantum sensing with nitrogen-vacancy centers in diamond, AVS Quantum Sci. **2**, 024701 (2020).

[32] M. M. Müller, R. S. Said, F. Jelezko, T. Calarco, and S. Montangero, One decade of quantum optimal control in the chopped random basis, Rep. Prog. Phys. **85** 076001 (2022).

[33] N. Khaneja, T. Reiss, C. Kehlet, T. Schulte-Herbrüggen, and S. J. Glaser, Optimal control of coupled spin dynamics: Design of NMR pulse sequences by gradient ascent algorithms, J. Magn. Reson. **172**, 296 (2005).

[34] S. Machnes, U. Sander, S. J. Glaser, P. de Fouquières, A. Gruslys, S. Schirmer, and T. Schulte-Herbrüggen, Comparing, optimizing, and benchmarking quantum-control algorithms in a unifying programming framework, Phys. Rev. A **84**, 022305 (2011).

[35] A. I. Konnov and V. F. Krotov, On global methods for the successive improvement of control processes, Avtomat. i Telemekh. **60**, 77 (1999) [Autom. Remote Control (Engl. Transl.) **60**, 1427 (1999)].

[36] M. H. Goerz, D. Basilewitsch, F. Gago-Encinas, M. G. Krauss, K. P. Horn, D. M. Reich, and C. P. Koch, Krotov: A Python implementation of Krotov's method for quantum optimal control, SciPost Phys. **7**, 080 (2019).

[37] N. Leung, M. Abdelhafez, J. Koch, and D. Schuster, Speedup for quantum optimal control from automatic differentiation based on graphics processing units, Phys. Rev. A **95**, 042318 (2017).

[38] P. Doria, T. Calarco, and S. Montangero, Optimal Control Technique for Many-Body Quantum Dynamics, Phys. Rev. Lett. **106**, 190501 (2011).

[39] N. Rach, M. M. Müller, T. Calarco, and S. Montangero, Dressing the chopped-random-basis optimization: A bandwidth-limited access to the trap-free landscape, Phys. Rev. A **92**, 062343 (2015).

[40] S. Machnes, E. Assémat, D. Tannor, and F. K. Wilhelm, Tunable, Flexible, and Efficient Optimization of Control Pulses for Practical Qubits, Phys. Rev. Lett. **120**, 150401 (2018).

[41] D. Lucarelli, Quantum optimal control via gradient ascent in function space and the time-bandwidth quantum speed limit, Phys. Rev. A **97**, 062346 (2018).

[42] J. J. W. H. Sørensen, M. O. Aranburu, T. Heinzel, and J. F. Sherson, Quantum optimal control in a chopped basis: Applications in control of Bose-Einstein condensates, Phys. Rev. A **98**, 022119 (2018).

[43] J. Zoller, Optimal quantum engineering, Ph.D. thesis, Faculty of Natural Sciences, University of Ulm, 2018.

[44] F. Hoeb, F. Angaroni, J. Zoller, T. Calarco, G. Strini, S. Montangero, and G. Benenti, Amplification of the parametric dynamical Casimir effect via optimal control, Phys. Rev. A **96**, 033851 (2017).

[45] F. Frank, T. Unden, J. Zoller, R. S. Said, T. Calarco, S. Montangero, B. Naydenov, and F. Jelezko, Autonomous calibration of single spin qubit operations, npj Quantum Inf. **3**, 48 (2017).

[46] R. Heck, O. Vuculescu, J. J. Sørensen, J. Zoller, M. G. Andreasen, M. G. Bason, P. Ejlertsen, O. Elíasson, P. Haikka, J. S. Laustsen, L. L. Nielsen, A. Mao, R. Müller, M. Napolitano, M. K. Pedersen, A. R. Thorsen, C. Bergenholtz, T. Calarco, S. Montangero, and J. F. Sherson, Remote optimization of an ultracold atoms experiment by experts and citizen scientists, Proc. Natl. Acad. Sci. USA **115**, E11231 (2018).

[47] M. Rossignolo, A. Marshall, T. Reisser, P. Rembold, A. Pagano, P. Vetter, R. Said, M. Müller, T. Calarco, S. Montangero, and F. Jelezko, QuOCS: A Quantum Optimal Control Suite (unpublished).

[48] N. Oshnik, P. Rembold, T. Calarco, S. Montangero, E. Neu, and M. M. Müller, Robust magnetometry with single nitrogen-vacancy centers via two-step optimization, Phys. Rev. A **106**, 013107 (2022).

[49] A. Omran, H. Levine, A. Keesling, G. Semeghini, T. T. Wang, S. Ebadi, H. Bernien, A. S. Zibrov, H. Pichler, S. Choi, J. Cui, M. Rossignolo, P. Rembold, S. Montangero, T. Calarco, M. Endres, M. Greiner, V. Vuletić, and M. D. Lukin, Generation and manipulation of Schrödinger cat states in Rydberg atom arrays, Science **365**, 570 (2019).

[50] T. Eichhorn, B. van den Brandt, P. Hautle, A. Henstra, and W. T. Wenckebach, Dynamic nuclear polarisation via the integrated solid effect II: Experiments on naphthalene-h_8 doped with pentacene-d_{14}, Mol. Phys. **112**, 1773 (2014).

[51] J. M. Binder, A. Stark, N. Tomek, J. Scheuer, F. Frank, K. D. Jahnke, C. Müller, S. Schmitt, M. H. Metsch, T. Unden, T. Gehring, A. Huck, U. L. Andersen, L. J. Rogers, and F. Jelezko, Qudi: A modular python suite for experiment control and data processing, SoftwareX **6**, 85 (2017).

[52] S. R. Hartmann and E. L. Hahn, Nuclear Double Resonance in the Rotating Frame, Phys. Rev. **128**, 2042 (1962).

[53] D. Stefanatos and E. Paspalakis, Speeding up adiabatic passage with an optimal modified Roland–Cerf protocol, J. Phys. A: Math. Theor. **53**, 115304 (2020).

[54] J. Roland and N. J. Cerf, Quantum search by local adiabatic evolution, Phys. Rev. A **65**, 042308 (2002).

[55] T. Caneva, T. Calarco, R. Fazio, G. E. Santoro, and S. Montangero, Speeding up critical system dynamics through optimized evolution, Phys. Rev. A **84**, 012312 (2011).

[56] S. van Frank, M. Bonneau, J. Schmiedmayer, S. Hild, C. Gross, M. Cheneau, I. Bloch, T. Pichler, A. Negretti, T. Calarco, and S. Montangero, Optimal control of complex atomic quantum systems, Sci. Rep. **6**, 34187 (2016).

[57] N. Malossi, M. G. Bason, M. Viteau, E. Arimondo, R. Mannella, O. Morsch, and D. Ciampini, Quantum driving protocols for a two-level system: From generalized Landau-Zener sweeps to transitionless control, Phys. Rev. A **87**, 012116 (2013).

[58] A. Van Strien and J. Schmidt, An EPR study of the triplet state of pentacene by electron spin-echo techniques and laser flash excitation, Chem. Phys. Lett. **70**, 513 (1980).

[59] A. Henstra and W. Wenckebach, Dynamic nuclear polarisation via the integrated solid effect I: Theory, Mol. Phys. **112**, 1761 (2014).

[60] B. Julsgaard, C. Grezes, P. Bertet, and K. Mølmer, Quantum Memory for Microwave Photons in an Inhomogeneously Broadened Spin Ensemble, Phys. Rev. Lett. **110**, 250503 (2013).

[61] T. Can, Q. Ni, and R. Griffin, Mechanisms of dynamic nuclear polarization in insulating solids, J. Magn. Reson. **253**, 23 (2015).

[62] A. Henstra, The integrated solid effect, Ph.D. thesis, Rijksuniversiteit te Leiden, 1990.

[63] F. Marquardt and A. Püttmann, Introduction to dissipation and decoherence in quantum systems, arXiv:0809.4403.

[64] C. Rackauckas and Q. Nie, DifferentialEquations.jl - A performant and feature-rich ecosystem for solving differential equations in Julia, J. Open Res. Software **5**, 15 (2017).

[65] T. Besard, C. Foket, and B. De Sutter, Effective extensible programming: Unleashing Julia on GPUs, IEEE Trans. Parallel Distrib. Syst. **30**, 827 (2019).

[66] T. Besard, V. Churavy, A. Edelman, and B. D. Sutter, Rapid software prototyping for heterogeneous and distributed platforms, Adv. Eng. Software **132**, 29 (2019).

[67] S. Bromberger *et al.*, JuliaGraphs/LightGraphs.jl: An optimized graphs package for the Julia programming language, 2017, https://doi.org/10.5281/zenodo.889971.

[68] J. Chen, J. Revels, and A. Edelman, Robust benchmarking in noisy environments, in *HPEC'16 Proceedings of the Twentieth IEEE High Performance Extreme Computing Conference* (IEEE, Waltham, MA, 2016).

[69] M. Besançon, VertexSafeGraphs.jl, 2019, https://github.com/matbesancon/VertexSafeGraphs.jl.

[70] P. K. Mogensen and A. N. Riseth, Optim: A mathematical optimization package for Julia, J. Open Source Software **3**, 615 (2018).

[71] C. Rackauckas and Q. Nie, Adaptive methods for stochastic differential equations via natural embeddings and rejection sampling with memory, Discrete Contin. Dyn. Syst. Ser. B **22**, 2731 (2017).

[72] Y. Ma, S. Gowda, R. Anantharaman, C. Laughman, V. Shah, and C. Rackauckas, ModelingToolkit: A composable graph transformation system for equation-based modeling, arXiv:2103.05244.

[73] C. Fieker, W. Hart, T. Hofmann, and F. Johansson, Nemo/Hecke: Computer algebra and number theory packages for the Julia programming language, in *Proceedings of the 2017 ACM on International Symposium on Symbolic and Algebraic Computation*, ISSAC '17 (ACM, New York, 2017), pp. 157–164.

[74] S. G. Johnson, QuadGK.jl: Gauss–Kronrod integration in Julia, 2016, https://github.com/JuliaMath/QuadGK.jl.

[75] M. Innes, Don't Unroll Adjoint: Differentiating SSA-form programs, arXiv:1810.07951.

[76] M. Udell, K. Mohan, D. Zeng, J. Hong, S. Diamond, and S. Boyd, Convex optimization in Julia, in *Proceedings of the 1st First Workshop for High Performance Technical Computing in Dynamic Languages* (IEEE, Piscataway, NJ, 2014), pp. 18–28.

[77] B. Legat, O. Dowson, J. D. Garcia, and M. Lubin, MathOptInterface: A data structure for mathematical optimization problems, INFORMS J. Comput. **34**, 671 (2022).

[78] M. Frigo and S. G. Johnson, The design and implementation of FFTW3, Proc. IEEE **93**, 216 (2005).

[79] E. L. Hahn, Spin Echoes, Phys. Rev. **80**, 580 (1950).

[80] T. Caneva, T. Calarco, and S. Montangero, Chopped randombasis quantum optimization, Phys. Rev. A **84**, 022326 (2011).

[81] F. Gao and L. Han, Implementing the Nelder-Mead simplex algorithm with adaptive parameters, Comput. Optim. Appl. **51**, 259 (2012).

[82] J. A. Nelder and R. Mead, A simplex method for function minimization, Comput. J. **7**, 308 (1965).

[83] S. Lloyd and S. Montangero, Information Theoretical Analysis of Quantum Optimal Control, Phys. Rev. Lett. **113**, 010502 (2014).